
COMPLEX VALUED DEEP OPERATOR NETWORK (DEEPONET) $[\mathcal{G}]$ FOR THREE DIMENSIONAL MAXWELL'S EQUATIONS: $\mathcal{G} \in \mathbb{C}^{m \times n}$

Qile Jiang

Division of Applied Mathematics
Brown University
Providence, RI 02906
qile_jiang@brown.edu

Marc Salvadori

Hypercomp Inc.
Westlake Village, CA 91362
msalvadori13@hypercomp.net

Dale Ota

Hypercomp Inc.
Westlake Village, CA 91362
dkota@hypercomp.net

Vijaya Shankar

Hypercomp Inc.
Westlake Village, CA 91362
vshankar@hypercomp.net

Khemraj Shukla*

Division of Applied Mathematics
Brown University
Providence, RI 02906
khemraj_shukla@brown.edu

ABSTRACT

The Maxwell's equations, a system of linear partial differential equations (PDEs), describe the behavior of electric and magnetic fields in time and space and is essential for many important electromagnetic applications. Although numerical methods have been applied successfully in the past, the primary challenge in solving these equations arises from the frequency of electromagnetic fields, which depends on the shape and size of the objects to be resolved. The frequency dictates the grid size used for the spatial discretization of the PDEs. Since the domain of influence for these equations is compactly supported, even a small perturbation in frequency necessitates a new discretization of Maxwell's equations, resulting in substantial computational costs. In this work, we investigate the potential of neural operators, particularly the Deep Operator Network (DeepONet) and its variants, as a surrogate model for Maxwell's equations. Existing DeepONet implementations are restricted to real-valued data in \mathbb{R}^n , but since the time-harmonic Maxwell's equations yield solutions in the complex domain \mathbb{C}^n , a specialized architecture is required to handle complex algebra. We propose a formulation of DeepONet for complex data, define the forward pass in the complex domain, and adopt a reparametrized version of DeepONet for more efficient training. We also propose a unified framework to combine a plurality of DeepONets, trained for multiple electromagnetic field components, to incorporate the boundary condition. As shown by computational experiments, our method significantly enhances the efficiency of predicting scattered fields from a spherical object at arbitrary high frequencies.

Keywords Maxwell's equations · Neural operators · Complex-valued neural network · Radar cross section

1 Introduction:

Electromagnetics is a fundamental subject that studies electric and magnetic fields, their interactions, and their effects on materials and systems, which is crucial to a variety of daily and industrial applications, including wireless communication [1, 2, 3], radar [4, 5, 6], and medical imaging [7, 8]. Central to this field are Maxwell's equations, which describe how electromagnetic waves propagate and respond to external charges and currents. However, analytical solutions in closed form are known for only a very limited number of special and trivial cases. This limitation has motivated the development of various high order numerical methods into solve the Maxwell's equation in time and frequency domain [9, 1, 10]. However, because the grid resolution depends on the size of the object being resolved, the numerical methods can become computationally demanding due to the high frequencies and small skin depth required

to resolve the small objects. To address this issue, we propose using a neural network-based approximate operator as a surrogate for the Maxwell’s equation solver.

Recently, computational problems in science and engineering have seen significant advancements through the application of deep learning methods. Commonly used neural network solvers can be broadly divided into two types: the first type focuses on learning mappings between input \mathbb{R}^m and output data \mathbb{R}^m , while the second type, known as neural operators, learns mapping between two functional spaces. In this work, we focus on the latter—neural operators [11, 12, 13]—which aim to approximate unknown operators that are often linked to the solution operator to differential equations. In mathematical terms, given data pairs (v, u) , where $v \in \mathcal{V}$ and $u \in \mathcal{U}$ belong to two function spaces, and a potentially nonlinear operator $\mathcal{G} : \mathcal{V} \mapsto \mathcal{U}$ such that $\mathcal{G}(v) = u$, the objective is to find a neural network approximation of \mathcal{G} , denoted by $\hat{\mathcal{G}}$, such that it can generalize to unseen data. By leveraging neural operators, we can efficiently replace highly complex and computationally intensive multiphysics systems and deliver functional outputs in real-time.

Deep Operator Network (DeepONet) [12] is a neural network based parametrized model for learning nonlinear operators and capturing the inherent relationships between input and output functions. DeepONets are built upon the universal operator approximation theorem [14, 12], which is an infinite dimensional analogue of the universal approximation theorem for neural networks [15, 16]. An architectural diagram of a DeepONet with the commonly used nomenclature for its components is shown in Figure 1. The DeepONet is a two-pronged deep learning network consisting of a branch network, which can take a multi-fidelity or multi-modal input [17, 18, 19, 20], and a trunk network encoded the independent variables defining the output space, e.g., in space–time coordinates. To recover the solution of a PDE the output of branch network is project on the output of trunk networks via an inner-product. DeepONet has seen success in solving complex problems in diverse scientific and engineering problems [21, 22, 23, 24, 25, 26], climate [27, 28, 29], and material science [30, 31, 18]. In Figure 1, we have shown fully connected architecture but any architecture can be used depending on the dimensionality of the training and testing data.

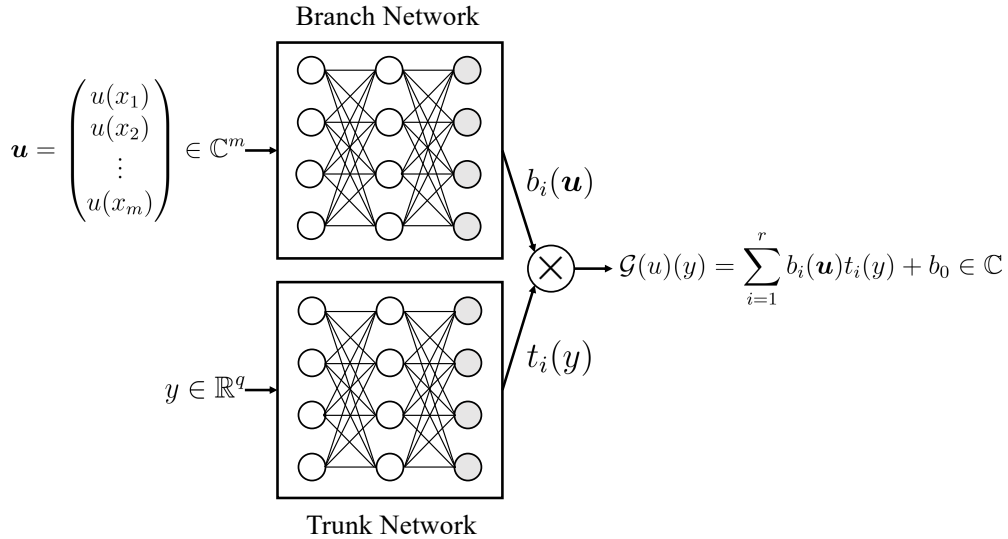


Figure 1: A schematic representation of a DeepONet, which is a neural operator trained to learn the mapping from the input function $u(x)$ to the output function $\mathcal{G}(u)(y)$, evaluated at $y \in \mathbb{R}^q$. DeepONet consists of two networks: a branch network, which processes the input function evaluations $[u(x_1), u(x_2), \dots, u(x_m)]^\top$, and a trunk network, which takes in the coordinates y .

All the existing applications of DeepONets focus on real-valued input and output data. However, many scientific problems involve complex-valued data, particularly in the solutions of important partial differential equations such as the Schrodinger equation [32, 33], Helmholtz equation [34], and Maxwell’s equations [35, 36]. Although, there are studies of solving Maxwell’s equation in 2D using PINNs [37, 38, 39, 40] but they consider the system with real valued solutions. To address the challenge of representing both the magnitude (m) and phase (φ) of a complex number $z = me^{i\varphi} \in \mathbb{C}$ and take advantage of the complex algebra, this work introduces the complex-valued DeepONet for learning operator mappings between complex-valued functions as input and output. Specifically, we demonstrate the effectiveness of using the complex-valued surrogate model for electromagnetic computations governed by the system of time-harmonic 3D Maxwell’s equations, where the DeepONet is leveraged to learn the general mapping from incident fields to the scattered fields parametrized by an arbitrary angular frequency.

To incorporate the the complex valued input and output in a neural network requires redefining all the three steps (1) Affine Transform (2) Non-linearity and (3) backpropagation. The first step requires matrix-vector product, which is well defined for complex valued matrices. The second step will require defining the non-linear activation function $f : \mathbb{C}^n \rightarrow \mathbb{C}^m$ for complex valued variables as domain and co-domain. This will require defining the new complex valued activation function. However, there are existing definitions of such functions and in this study we use the definition proposed by [41]. In third step we require computing the gradient of loss function with respect to complex parameters of neural network. To achieve this efficiently, we have used Wirtinger calculus [42]. The usage of complex valued neural network is not common, but a few studies have shown great promise of using complex valued model for classification [43] and regression [44, 45, 46] problems.

This paper is structured as follows: In section 2, we present the definition of the problem, governing equations, the geometry of the domain, and the data generation techniques used to train n the model. Next, in section 3, we describe the architecture and forward passes for the complex-valued DeepONet. In addition, we adapts a two-step training approach to reparametrize the complex-valued network and demonstrate how separate DeepONets can be combined to enforce the boundary conditions for a perfect electric conductor (PEC). Lastly, in section 4, we highlight the superior results of the complex-valued model compared to its real-valued counterpart, along with the post-processed radar cross-section (RCS) results.

2 Problem setup

The computational domain considered here is a sphere with the surface being perfectly electrically conductive materials (PEC). In this section, we define the problem setup, governing equations, and numerical methods used to generate the data for the given 3D domain.

2.1 System of time-harmonic Maxwell's equations

In this work, we devise the DeepONet to address the direct scattering problem, which is commonly encountered in various important electromagnetic applications and system is governed by Maxwell's equations, which reads as follows,

$$-i\omega\epsilon\mathbf{E} - \nabla \times \mathbf{H} = 0 \quad \text{in } \Omega, \quad (1)$$

$$-i\omega\mu\mathbf{H} + \nabla \times \mathbf{E} = 0 \quad \text{in } \Omega, \quad (2)$$

where \mathbf{E} and \mathbf{H} are the electric and magnetic fields, ω is the angular frequency of the radiation, ϵ and μ are respectively the electric and magnetic permeability of the material in the computational domain Ω . Ω is Lipschitz and piecewise smooth.

In Ω , the complex time harmonic electric field phasor \mathbf{E} satisfies

$$\nabla \times \mu^{-1} \nabla \times \mathbf{E} - \kappa^2 \epsilon \mathbf{E} = 0 \quad \text{in } \Omega, \quad (3)$$

where $\kappa = \omega \sqrt{\epsilon_0 \mu_0}$ is the wave number.

Additionally, we assume the following generalized impedance boundary condition on $\partial\Omega$, which is expressed as,

$$\mathbf{v} \times \mu^{-1} \nabla \times \mathbf{E} - ikZ\mathbf{E}_T = Q(\mathbf{v} \times \mu^{-1} \nabla \times \mathbf{E} + ikZ\mathbf{E}_T) + \mathbf{g} \quad \text{on } \partial\Omega, \quad (4)$$

where, $\mathbf{E}_T = \mathbf{v} \times (\mathbf{E} \times \mathbf{v})$ is the tangential component of the electric field, Q is a complex scalar-valued function on the boundary with $|Q| \leq 1$, and \mathbf{g} is a prescribed source function. The $Z(\geq 0)$ is defined on the boundary $\partial\Omega$, and we take it to be $Z = \sqrt{|\mu|/|\epsilon|}$. Note that the choice $Q = 1$ corresponds to a Perfect Electric Conductor (PEC) type boundary condition for the waves scattered of the PEC surface and recovered as

$$\mathbf{E}_T = -\frac{1}{2i\kappa Z} \mathbf{g}. \quad (5)$$

For scattering applications, we assume that we have a bounded scatterer which can be impenetrable (for example, with an impedance or PEC boundary condition) or penetrable (for example, a dielectric) occupying a domain D in the interior of the computational domain Ω . A known incident field \mathbf{E}^i impinges on the scatterer and creates an outgoing scattered field \mathbf{E}^s . Then, the total field $\mathbf{E} = \mathbf{E}^i + \mathbf{E}^s$ satisfies the homogeneous Maxwell system 1. The incident field \mathbf{E}^i is assumed to satisfy the background Maxwell's equations in the neighborhood of D , which is expressed as

$$\nabla \times \nabla \times \mathbf{E}^i - k^2 \mathbf{E}^i = 0. \quad (6)$$

In this work, we consider the incident plane wave $\mathbf{E}^i = \mathbf{E}_0^i \exp(ik\mathbf{d} \cdot \mathbf{x})$, where the real direction vector \mathbf{d} satisfies $\|\mathbf{d}\| = 1$ and the real polarization $\mathbf{E}_0^i \neq 0$ is such that $\mathbf{E}_0^i \cdot \mathbf{d} = 0$.

The direct scattering problem involves determining \mathbf{E}^s based on the known incident field \mathbf{E}^i . Traditionally, this requires complex numerical simulations to solve the governing equations. Since these equations depend on the angular frequency and the incident fields can vary with frequency, computing the scattered field for each case using conventional methods is very computationally expensive. To resolve the frequency, we will require multiple grid points for the smaller wavelength. That requires solving a linear system of equation of size N^3 where N defines the number of degrees of freedom in the simulations. To address this, we developed a complex-valued DeepONet that efficiently learns the general operator mapping from both frequency and incident field to the total field, which can significantly improve computational efficiency for scattering problems in industrial applications.

2.2 Computational domain and data generation

The computational domain of the problem, shown in Figure 2, consists of a homogeneous metallic sphere with a radius of $r = 1$ m (shown as green sphere) and an outer boundary positioned at a distance of 3λ from the metallic sphere, where λ (m) is the wavelength given as

$$\lambda = \frac{c}{f} \quad (7)$$

where $c = 3 \times 10^8$ m/s is the speed of light and f (Hz) is the maximum frequency of the electromagnetic wave considered in this problem.

The computational domain is discretized by tetrahedral meshes with 3 cells per wavelength (λ) and is presented in Figure 2b. Two different problems are considered in this work. For the first study, we consider electromagnetic fields with a maximum frequency of 0.6 GHz. The corresponding wave length $\lambda = 0.5$ m and the sphere surface resolution is $\frac{1}{6}$ m. Under this configuration, the sphere surface is discretized into 1004 triangular facets, the outer boundary is discretized into 1408 triangular facets, and the volume cells are discretized into 25,042 tetrahedral elements with a maximum cell size of 6λ . For a more advanced second study, we consider a much higher maximum frequency of 4.77 GHz, so the corresponding wavelength $\lambda = 6.28 \times 10^{-2}$ m, the sphere surface resolution is 2.10×10^{-2} m, and the sphere is discretized into 137,388 triangular facets. In the second case, we test the scalability of the proposed surrogate model to a significantly larger dataset required to resolve the higher frequency and smaller wavelength.

The training dataset contains the incident fields $\mathbf{E}^i(x, y, z; f)$ impinging the sphere at different incidence angles, frequencies (f), and spatial locations of sensors, which in this case are coordinates of vertices (x, y, z) of the tetrahedral and triangles. The output of the DeepONet is the total field $\mathbf{E}(x, y, z; f)$. To generate the training and testing data, we utilized the Ultra Weak Variational Formulation (UWVF) method [47, 48, 49] to solve the system described by Equation 1. UWVF is a special case of a Trefftz-discontinuous Galerkin (Trefftz-DG) method provided the scattering medium is lossless. The UWVF approach uses an unstructured finite element computational grid and a superposition of plane wave solutions of Maxwell’s equations on each tetrahedral element [50]. UWVF has been found to be efficient for approximating solutions of Maxwell’s equations for a wide range of test problems as shown by Lahivaara et al.[51].

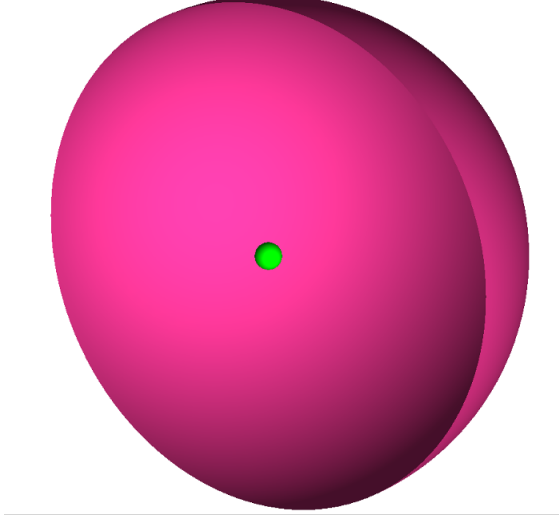
3 Surrogate Modeling

In this section, we formulate the neural operators, specifically the DeepONet as a surrogate model to solve the scattering problem described in subsection 2.1. We first formulate the setup for a vanilla real-valued DeepONet and then design a complex-valued variant to more effectively address the time-harmonic Maxwell’s equations. Furthermore, we propose methods to enforce the boundary conditions for the total field, ensuring that the resulting Physics-Informed Complex-Valued DeepONet satisfies these constraints, thus improving the interpretability of the model.

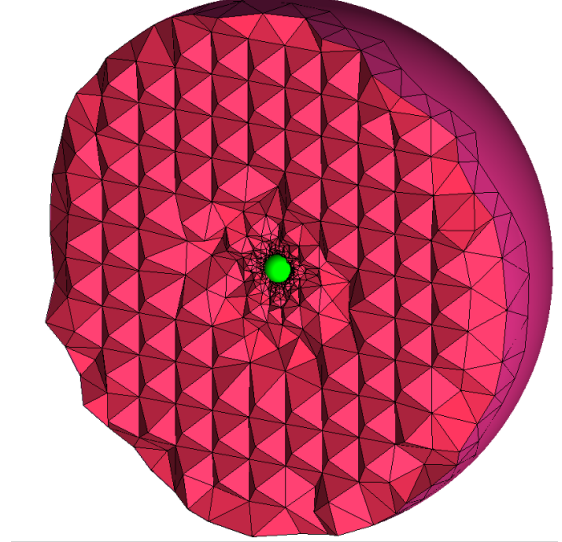
3.1 Formulation of a real valued DeepONet

The DeepONet [12] is a neural operator used to learn the underlying mapping between spaces of function from data, based on the universal approximation theorem of operators [14]. Specifically, we denote the input function by $u : x \mapsto u(x)$, defined on the domain $D \subset \mathbb{R}^n$, and the output function by $v : y \mapsto v(y)$, defined on domain $\Omega \subset \mathbb{R}^m$. Let \mathcal{U} and \mathcal{V} be the function spaces that contain u and v , respectively. The mapping from the input function u to the output function v is denoted by an operator:

$$\mathcal{G} : \mathcal{U} \ni u \mapsto v \in \mathcal{V}. \quad (8)$$



(a) Computational domain with the outer boundary and metallic sphere.



(b) Meshed geometry of the computational domain.

Figure 2: Computational domain used for electromagnetic simulations. Subfigure (a) shows the simplified outer boundary with a metallic sphere (in green color) at the center. Subfigure (b) shows crinkled view of the tetrahedral meshes used to discretize the computational domain show in (a).

The basic DeepONet consists of two primary building blocks: the **trunk network**, which takes the coordinates $y \in \Omega$ as input and outputs the corresponding basis functions; and the **branch network**, which takes the discretized input function u as input. Here, u is evaluated at m arbitrary spatial coordinates $\{x_1, x_2, \dots, x_m\}$ to obtain pointwise evaluations $\mathbf{u} = \{u(x_1), u(x_2), \dots, u(x_m)\}$ that will serve as the input to the branch network. The continuous approximation of the output performed by DeepONet reads as

$$v(y) = \mathcal{G}(u)(y) \approx \sum_{i=1}^r b_i(\mathbf{u})t_i(y) + b_0, \quad (9)$$

where b_i and t_i are the r -dimensional outputs of the branch and trunk networks, respectively. $b_0 \in \mathbb{R}$ is a trainable bias term. By evaluating the network's output at the coordinates $\{y_1, y_2, \dots, y_q\}$, we obtain the continuous prediction of \mathbf{v} projected at \mathbf{y} as $[v(y_1), v(y_2), \dots, v(y_q)]^\top$, which approximated the ground truth data.

The solutions to the time-harmonic Maxwell's equations are parameterized by the angular frequency. Therefore, our goal is to learn the operator with two inputs $\mathcal{G} : (\mathbf{E}^i; f) \mapsto \mathbf{E}$, where $\mathbf{E}^i \in \mathbb{C}^3$ is the incident field, $f \in \mathbb{R}$ is the angular frequency, and $\mathbf{E} \in \mathbb{C}^3$ is the total field. Two branch networks, b^{inc} and b^{freq} , are used to encode the incident field and the frequency separately. Additionally, since the incident field is complex-valued, its real and imaginary parts are learned separately in the real-valued DeepONet. In particular, we consider real and imaginary component of a complex valued input and output pair as two separate features and labels, respectively. The total field evaluated at $y \in \mathbb{R}^3$ is given as $\mathbf{E}(y) = \mathcal{G}(\mathbf{E}^i; f)(y) \approx \sum_{i=1}^r b_i^{inc}(\mathbf{E}^i)b_i^{freq}(f)t_i(y) + b_0$.

3.2 Formulation of a Complex-valued DeepONet

In a real-valued neural network, a complex number $z \in \mathbb{C}$ is represented by 2 real-valued channels, each channel containing the real and imaginary components, $\Re(z)$ and $\Im(z)$ respectively. For example, to learn the mapping $x + iy \mapsto a + ib$ with N samples of data, the real-value neural network learns the mapping between N real-valued 2D vectors

$$\begin{bmatrix} x_1 & y_1 \\ x_2 & y_2 \\ \vdots & \vdots \\ x_N & y_N \end{bmatrix} \mapsto \begin{bmatrix} a_1 & b_1 \\ a_2 & b_2 \\ \vdots & \vdots \\ a_N & b_N \end{bmatrix}, \quad (10)$$

and then recombines the real part a_j and imaginary part b_j to produce the complex-valued output $a_j + ib_j$. However, this separate representation does not respect the phase information that is captured by complex algebra. In contrast, a

complex-valued neural network directly learns the complex-valued mapping

$$\begin{bmatrix} x_1 + iy_1 \\ x_2 + iy_2 \\ \vdots \\ x_N + iy_N \end{bmatrix} \mapsto \begin{bmatrix} a_1 + ib_1 \\ a_2 + ib_2 \\ \vdots \\ a_N + ib_N \end{bmatrix}.$$

Previous research [43, 44, 45, 46] has shown that the real-valued approach to inherently complex-valued data performs poorly in terms of efficient architecture, convergence, and generalization ability. Since the solutions to the time-harmonic Maxwell’s equations are inherently complex-valued, we address this challenge by implementing the DeepONet in the complex domain to learn the mapping between a complex-valued fields. The complex-valued DeepONet retains the same structure as the basic DeepONet, but both the input and output functions are complex-valued, and all calculations are performed using the `complex64` datatype.

In a complex-valued neural network (CVNN), the forward pass for a given layer is represented as

$$\begin{aligned} \mathbf{h} &= \mathbf{W}\mathbf{x} + \mathbf{b}, \\ \mathbf{z} &= \sigma(\mathbf{h}) \end{aligned} \quad (11)$$

where $\mathbf{x} \in \mathbb{C}^n$ is the input vector, $\mathbf{W} \in \mathbb{C}^{m \times n}$ is the complex weight matrix, $\mathbf{b} \in \mathbb{C}^m$ is the complex bias vector, and $\sigma(\cdot)$ is the activation function.

Two types of activation functions exist for CVNN. First, split activation functions, where real and imaginary parts are treated independently; second, fully complex activation function, where real and imaginary parts are treated as a single entity. A complex-valued activation function cannot be bounded and analytic everywhere at the same time, because Liouville’s theorem states that such functions are constant. Due to the computation complexity and the difficulty in fulfilling Liouville’s theorem, fully complex activation functions are less frequently studied than split-type activation functions [52].

In complex-valued DeepONet, we adopt a split ReLu activation function, denoted $\mathbb{C}\text{ReLu}$, that applies ReLu to the real and imaginary parts of the complex-valued input $z \in \mathbb{C}$

$$\mathbb{C}\text{ReLu}(z) = \max(0, \Re(z)) + i \cdot \max(0, \Im(z)). \quad (12)$$

The $\mathbb{C}\text{ReLu}$ function satisfies the Cauchy-Riemann equations when both the real and imaginary parts are at the same time either strictly positive or strictly negative but is not bounded.

Additionally, to enhance DeepONet’s ability to capture oscillatory patterns in the functions, a periodic feature-extension layer is added to the trunk network input \mathbf{y} . This layer computes multiple sine and cosine values of the input before passing the augmented features to the rest of the trunk network. The periodic feature extension is expresses as

$$\text{periodic feature of } \mathbf{y} = \mathbf{y} + \sum_{n=1}^N \sin(n\mathbf{y}) + \cos(n\mathbf{y}), \quad (13)$$

where N is the extended feature size.

Finally, a real-valued loss function for the complex-valued DeepONet is designed to account for both the real and imaginary parts of the output. As an example, let $E_x^{NN}(x, y, z)$ denote the DeepONet prediction of the x -component of the incident electric field, evaluated at the coordinate (x, y, z) , and let $\bar{E}_x(x, y, z)$ denote ground truth total field. The mean squared error (MSE) for the complex data is defined as follows

$$\text{MSE}(E_x^{NN}, \bar{E}_x) = \frac{1}{N} \sum_{(x,y,z) \in \Omega} [(\Re(E_x^{NN}(x, y, z)) - \Re(\bar{E}_x(x, y, z)))^2 + (\Im(E_x^{NN}(x, y, z)) - \Im(\bar{E}_x(x, y, z)))^2], \quad (14)$$

where N is the total number of data points in the computational domain Ω .

The same MSE function is used for all other components of the electric and magnetic fields. A separate DeepONet is implemented for each of the six components of the electric and magnetic fields to minimize their losses separately. Our implementation utilizes the Complex Valued Neural Network package [53] to simplify the workflow.

3.3 Imposing the PEC boundary condition

To impose the physics on the proposed DeepONet architecture, we adopt the approach of soft constraint. Since, the metallic scatterer examples studied in this work are perfect electric conductors (PEC), and the electric field on the

surface of a PEC scatterer is orthogonal to the conductor. Therefore, the PEC boundary condition entails that $\mathbf{n} \times \mathbf{E} = 0$, where \mathbf{n} is the normal vector to the scatterer surface and \mathbf{E} is the total field. Previous research such as [54, 55] has proposed ways of integrating such first-principle-informed conditions directly into the architecture of neural networks. Due to the high-dimensional training data in our problem, we instead incorporate the PEC boundary condition directly into the loss function.

Since a separate complex-valued DeepONet is trained for each field component, the boundary condition is enforced in two stages, as illustrated in Figure 3. First, DeepONets are trained independently and concurrently for the components $E_x, E_y, E_z, H_x, H_y,$ and H_z , with each model minimizing the data-driven loss as defined in Equation 14. Once the data-driven loss for each component is minimized sufficiently, the trained models are saved. Next, to impose the boundary condition on the electric field, previously trained models for $E_x, E_y,$ and E_z are loaded and retrained jointly. During this phase of training, the PEC boundary condition is introduced into the loss function as an additional term. The loss function for this retraining step is defined as

$$L = w_1 \|\mathbf{n} \times \mathbf{E}^{NN}\|_2^2 + w_2 (\text{MSE}(E_x^{NN}, \bar{E}_x) + \text{MSE}(E_y^{NN}, \bar{E}_y) + \text{MSE}(E_z^{NN}, \bar{E}_z)), \quad (15)$$

where $\|\cdot\|_2$ represents the L_2 norm. The weights w_1 and w_2 control the balance between the boundary-condition-informed and data-driven losses and are adjusted during retraining to ensure both the boundary condition and the data loss are satisfied.

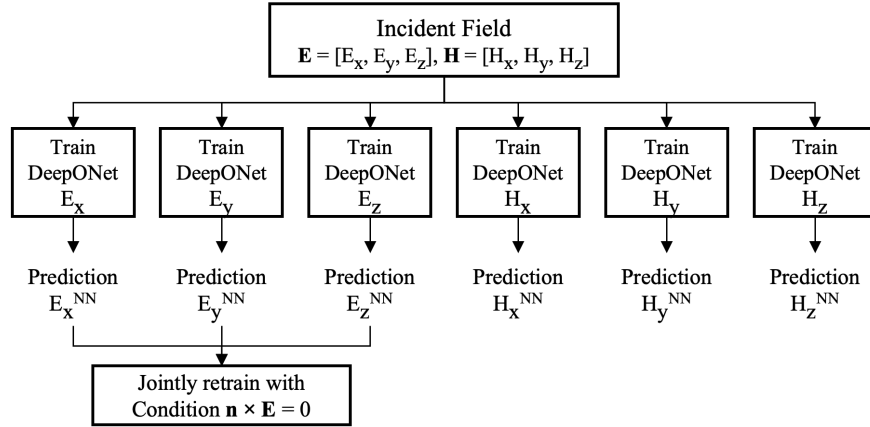


Figure 3: Illustration of the two-stage process for training a combination of DeepONet models for different field components to impose the PEC boundary condition $\mathbf{n} \times \mathbf{E} = 0$ on the electric field.

3.4 Reparametrization of the Complex-valued DeepONet

In a complex-valued DeepONet, the trunk network serves as the basis functions for the output, while the branch network provides the coefficients. In [56], the study introduced a two-step training method to simplify the optimization of the DeepONet: the first step is to determine the basis representation through the trunk network and find the corresponding coefficients without involving the branch network; and in the second step, the branch network learns these coefficients. We can extend this method into the complex domain, as the operations are well-defined for complex matrices.

Specifically, let $\mathbf{u} = \{u_k\}_{k=1}^K$ be a set of complex-valued input functions from the function space \mathcal{U} , and let $v_k(\cdot) = \mathcal{G}[u_k](\cdot)$ be the corresponding complex-valued output functions in the space \mathcal{V} . The branch network, denoted as $\mathbf{b}(\cdot; \theta)$, is a CVNN with L_b layers and an output dimension of N

$$\mathbf{b}(\cdot; \theta) = (b_0(\cdot; \theta), \dots, b_N(\cdot; \theta))^T \in \mathbb{C}^N, \quad (16)$$

where θ represents the parameters of the branch network. Similarly, the trunk network, denoted as $\mathbf{t}(y; \mu)$, is a vector-valued CVNN with L_t layers defined for $y \in \Omega_y \subset \mathbb{C}^{d_y}$ with the same output dimension

$$\mathbf{t}(y; \mu) = (1, t_1(y; \mu), \dots, t_{N-1}(y; \mu))^T \in \mathbb{C}^N, \quad (17)$$

where μ represents the parameters of the trunk network.

The output of the complex-valued DeepONet is given by the element-wise product of the branch and trunk networks:

$$O_{\text{net}}[\mathbf{u}, \Theta] = \mathbf{t}^T(y; \mu) \mathbf{b}(\mathbf{u}; \theta), \quad (18)$$

where $\Theta = \{\theta, \mu\}$ is the set of all trainable parameters in the DeepONet. When training the DeepONet with a batch of input functions $\{u_k\}_{k=1}^K$ and trunk net coordinates $\{y_i\}_{i=1}^m$, we denote

$$\mathbf{T}(\mu) := \begin{bmatrix} \mathbf{t}^\top(y_1; \mu) \\ \vdots \\ \mathbf{t}^\top(y_m; \mu) \end{bmatrix} \in \mathbb{C}^{m \times N}, \quad (19)$$

$$\mathbf{B}(\theta) := [\mathbf{b}(u_1; \theta), \dots, \mathbf{b}(u_K; \theta)] \in \mathbb{C}^{N \times K}, \quad (20)$$

and the matrix of target outputs $\mathbf{V} := [\mathbf{v}_1, \dots, \mathbf{v}_K] \in \mathbb{C}^{m \times K}$.

In the first step of the two-step method, the trunk network is trained by solving the following optimization problem:

$$\min_{\mu, A} \mathcal{L}(\mu, A) := \|\mathbf{T}(\mu)A - \mathbf{V}\|_2^2, \quad (21)$$

where $A \in \mathbb{C}^{N \times K}$ is a complex matrix that temporarily replaces the branch net during the phase. Let (μ^*, A^*) be an optimal solution to this problem and let $\mathbf{T}(\mu^*)$ be full rank. We can perform a QR-factorization of the optimized trunk network, i.e., $QR = \mathbf{T}(\mu^*)$, where $Q \in \mathbb{C}^{m \times m}$ is a unitary matrix (the conjugate transpose $Q^\dagger = Q^{-1}$) and $R \in \mathbb{C}^{m \times N}$ is an upper triangular matrix.

In the second step, we train the branch network to fit the product RA^* . This is done by solving the optimization problem:

$$\min_{\theta} \|\mathbf{B}(\theta) - RA^*\|_2^2. \quad (22)$$

Assuming θ^* to be the optimal solution, the fully trained branch network is then given by $\mathbf{b}(\cdot; \theta^*)$.

3.5 Sampling of the input space

The performance of the DeepONet is sensitive to the values of the angular frequency selected for training. However, sampling a broad range of frequencies is inefficient and impractical due to the computational expense of generating large training datasets. Thus, an efficient data acquisition strategy is required to select frequencies that maximize information gain and enhance model performance with fewer samples. Traditional methods for sampling training frequencies within a given interval $[f_{min}, f_{max}]$ such as uniform sampling, Latin hypercube sampling, and random sampling do not account for the sensitivity of the model's predictions to input frequencies. Instead, we employ the method of acquisition function [57] to sample input space for the training of complex-valued DeepONet.

An acquisition function is a criterion used in active learning to select the next data point to be sampled. The motivation behind using an acquisition function is to efficiently explore the input space, especially in scenarios involving rare and extreme events, and construct a more generalizable model with fewer samples. To implement the acquisition function, we employ an ensemble of N DeepONets, where the mean solution of the ensemble, $\bar{G}(f)$, with respect to input frequency f is given by:

$$\bar{G}(f) = \frac{1}{N} \sum_{n=1}^N G_n(f),$$

where $G_n(f)$ denotes the prediction of the n -th DeepONet in the ensemble. The predictive variance is then calculated as

$$\sigma^2(f) = \frac{1}{N-1} \sum_{n=1}^N |G_n(f) - \bar{G}(f)|^2. \quad (23)$$

which gives a real scalar representing the spread of the complex-valued predictions. We then define the acquisition function to be this predictive variance

$$a(f) = \sigma^2(f), \quad (24)$$

During the training, Monte Carlo optimization is employed to find the samples where the predictive variance is the greatest. This is done by generating a set of random samples from the input space using Latin Hypercube Sampler and evaluating them with the DeepONet ensemble to identify the sample that maximizes the acquisition function. The identified sample is then incorporated into the training dataset. This method prioritizes sampling points with the highest predictive variance, so that the training focuses on regions of the input space where the model is most uncertain and provides the greatest gain for learning about the underlying system.

4 Results

In this section we show the performance of the proposed DeepONet architecture for the Maxwell’s equation.

4.1 A comparison between Real valued DeepONet, Complex value DeepONet and Reparametrized complex valued DeepONet

To demonstrate the superior performance of the complex-valued DeepONet compared to the vanilla real-valued DeepONet, we used similar architectures for both models, training them on the same 80 frequencies and testing on 21 frequencies sampled from a range of [0.05, 0.6] GHz. The hyperparameters for both models used in our experiments are summarized in Table 1. For the real-valued DeepONet, the real and imaginary parts of a function are trained separately and then combined into a complex number for comparison against the ground-truth data. The training loss histories of the two models are plotted in Figure 4, with the dotted line representing the real-valued DeepONet and the solid line representing the complex-valued DeepONet. The loss stabilizes at around 10,000 epochs, with the complex-valued DeepONet achieving superior training loss across all components of the field. The final testing results are summarized in Figure 4, which shows that the reparametrized complex-valued DeepONet, trained using the two-step method, exhibits the best testing performance. The complex-valued models significantly outperform the vanilla real-valued model by decreasing the error with a factor ranging from 5-7 times. In terms of inference speed, the UWVF numerical solver takes 15 minutes to predict one frequency using 192 cores. In comparison, the complex-valued DeepONet predicts a single frequency in 1.16 seconds on a 24-core CPU or 0.10 seconds on an Nvidia Titan RTX GPU.

Figure 5 shows the correlation between predicted and true total fields. Strong diagonal alignment demonstrates high prediction accuracy for both the electric and magnetic fields. Figure 6 shows the predictions of the total electric and magnetic fields by the complex-valued model at a testing frequency of 0.402 GHz. The pointwise absolute errors between the ground truths and predictions are plotted in green, with small errors primarily occurring in areas where the regularity of the function is poor. The model is shown to generalize well to the testing frequencies.

Table 1: Hyperparameters of the vanilla real-valued and complex-valued DeepONets

Real Valued DeepONet		Complex Valued DeepONet	
Branch net architecture	[1004, 64, 64, 64, 64, 200]	Branch net architecture	[1004, 64, 64, 64, 64, 200]
Trunk net architecture	[3, 64, 64, 64, 200]	Trunk net architecture	[3, 64, 64, 64, 200]
Activation	ReLU	Activation	CReLU
Latent dimension r	200	Latent dimension r	200
Optimizer	Adam	Optimizer	Adam
Learning rate	Polynomial learning rate schedule, with initial and end learning rate at 10^{-3} and 10^{-4} , respectively	Learning rate	Polynomial learning rate schedule, with initial and end learning rate at 10^{-3} and 10^{-4} , respectively
Training epochs	30000	Training epochs	30000

In the second example, we tested the capability of the complex-valued DeepONet to handle electromagnetic fields with a much higher maximum frequency of 4.77 GHz. To resolve the higher frequencies and smaller wavelengths, the computational domain is discretized into a finer mesh as described in subsection 2.2 and the incident field is evaluated on 137,388 sensor locations. To accommodate this increase, a larger DeepONet model is created with a branch network input dimension of 137,388 and the number of neurons per layer raised to 128. The number of hidden layers and other model hyperparameters are unchanged. After training for 100,000 epochs, the training and testing relative L_2 losses are presented in Table 2. These results show that the complex-valued DeepONet can effectively scale to a much larger dataset to handle high-frequency fields without compromising its accuracy or altering training routine.

4.2 Acquisition functions for sampling the input space

The acquisition function is used to efficiently select training frequencies for the complex-valued DeepONet. We consider the frequency range of [0.05, 0.6] GHz. An initial set of 5 uniformly distributed frequencies in this range are selected for training an ensemble of 3 DeepONets. Then, an additional 15 frequencies are acquired to maximize information gain as determined by the acquisition function. The trained model is subsequently tested on 80 unseen samples.

For a comparison, we also train the vanilla complex-valued DeepONet to randomly select 20 training samples, and both models are trained for 30000 epochs. The final testing losses in Figure Figure 8 indicate that the acquisition

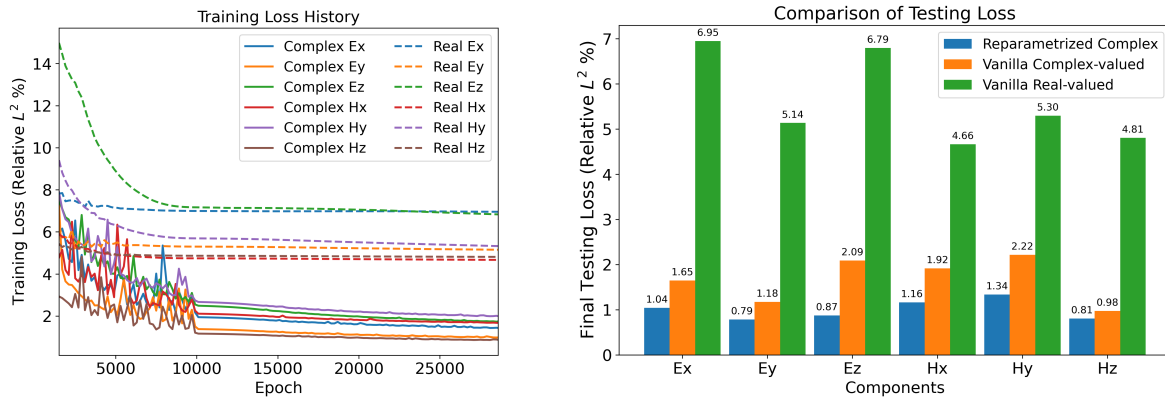


Figure 4: Left sub figure shows training loss history for each electromagnetic field using complex-valued DeepONets (solid line) and real-valued DeepONets (dotted line), starting from 500 epochs. This clearly shows the improvement of the accuracy for complex valued DeepONet significantly. The right subfigure shows Testing performance of DeepONets (the complex-valued DeepONet, and the reparametrized complex-valued DeepONet) at testing frequencies. The plot infer a superior performance of complex valued DeepONet over real valued DeepONet.

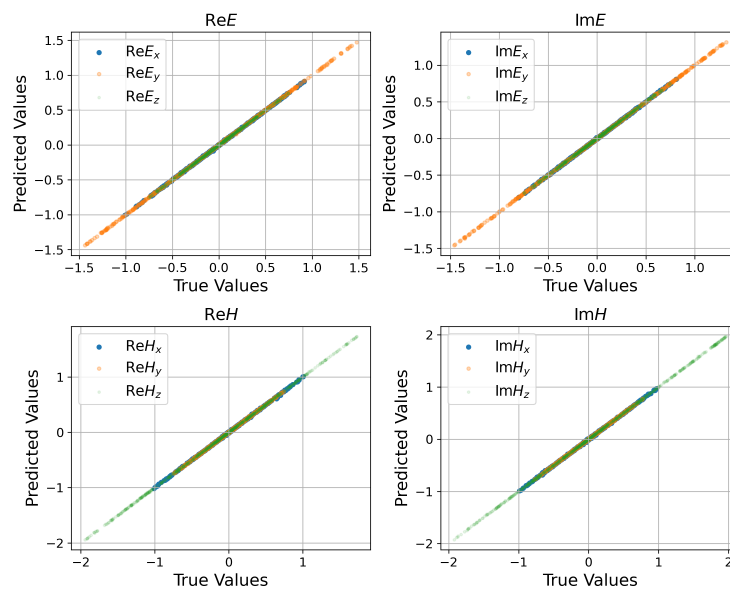


Figure 5: Scatter plots showing the correlation between predicted and true values for the real ($\Re(E)$) and imaginary ($\Im(E)$) components of the electric field, and for the real ($\Re(H)$) and imaginary ($\Im(H)$) components of the magnetic field. Strong diagonal alignment demonstrates high prediction accuracy for both fields.

method significantly outperforms the original complex-valued DeepONet in predicting unseen testing data across all components of the electric and magnetic fields. Figure 8 illustrates the frequencies that are acquired for training and testing with their respective relative L^2 losses, which shows that with a very limited training dataset, our model can still generalize well to unseen testing data.

4.3 Deponent as surrogate for computing radar cross section (RCS) results

The radar cross section (RCS) of a target is an equivalent area that reflects the transmitted power in a given direction. In many applications, the RCS derived from far-field patterns of the scattered wave is often the quantity of interest. The

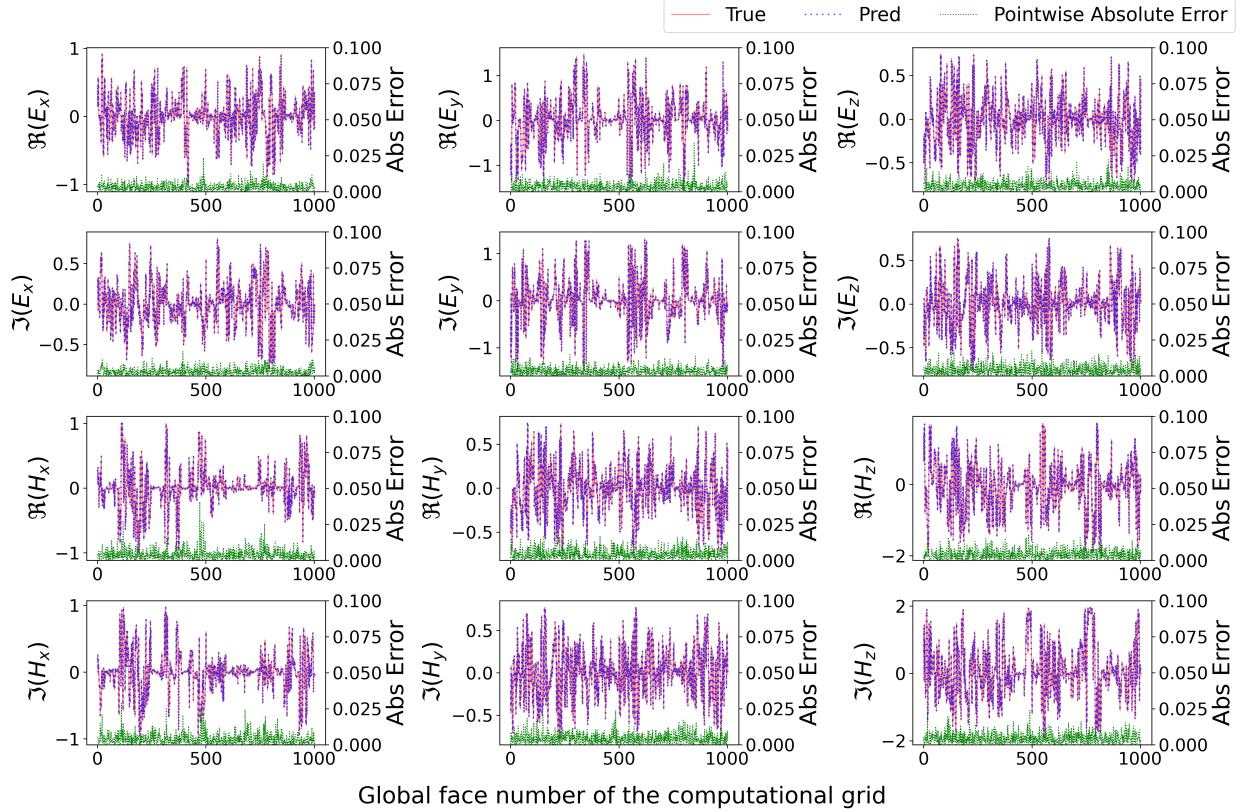


Figure 6: A comparison between ground truth (red solid line) and prediction (blue dotted line) of each component of the electric and magnetic fields at a frequency of 0.402 GHz. The pointwise absolute error between the true and predicted values is plotted by the green line. Figures show a very good agreement between actual and inferred electromagnetic field.

Table 2: Relative L_2 errors for training and testing for complex-valued DeepONet on a much larger dataset with high-frequency fields up to 4.77 GHz

Component	Training L_2 %	Testing L_2 %
E_x	2.94	3.01
E_y	1.34	1.33
E_z	1.99	1.97
H_x	1.78	1.78
H_y	1.15	1.15
H_z	2.74	2.71

electric far-field pattern \mathbf{E}_∞ is defined in spherical coordinates (r, θ, ϕ) as

$$\mathbf{E}(r, \theta, \phi) \approx \mathbf{E}_\infty(\theta, \phi) \frac{e^{i\omega\sqrt{\mu\epsilon}r}}{r}, \quad (25)$$

when $r \rightarrow \infty$ [48].

The RCS is expressed as the ratio of the power density of the scattered field evaluated in the far-field to the incident power density times the area of a sphere of radius r , in the limit $r \rightarrow \infty$. The monostatic and bistatic radar cross sections (RCS), computed using field predictions from the complex-valued DeepONet, are presented in Figure 9. For these results, the DeepONet was trained on 60 samples and tested on 40 samples. In Figure 9, the monostatic RCS is calculated at an azimuth angle of $\phi = 0$ for frequencies ranging from 0.05 to 0.6 GHz, while the bistatic RCS is shown for a frequency of 0.281 GHz with ϕ varying from 0 to 360 degrees. For both monostatic and bistatic RCS calculations, the analytical Mie-series solutions are used as the ground truth for comparison. The results of RCS ensures the accuracy

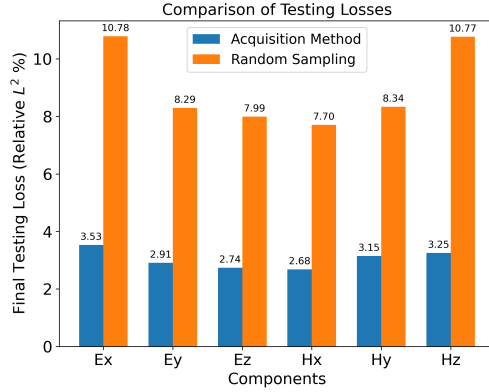


Figure 7: Comparison of relative L^2 errors in testing predictions for each component of the electromagnetic field using two sampling methods: the acquisition function sampling method and the random sampling method. Both methods are applied to the vanilla complex-valued DeepONet, trained with 20 data samples and tested with 81 samples.

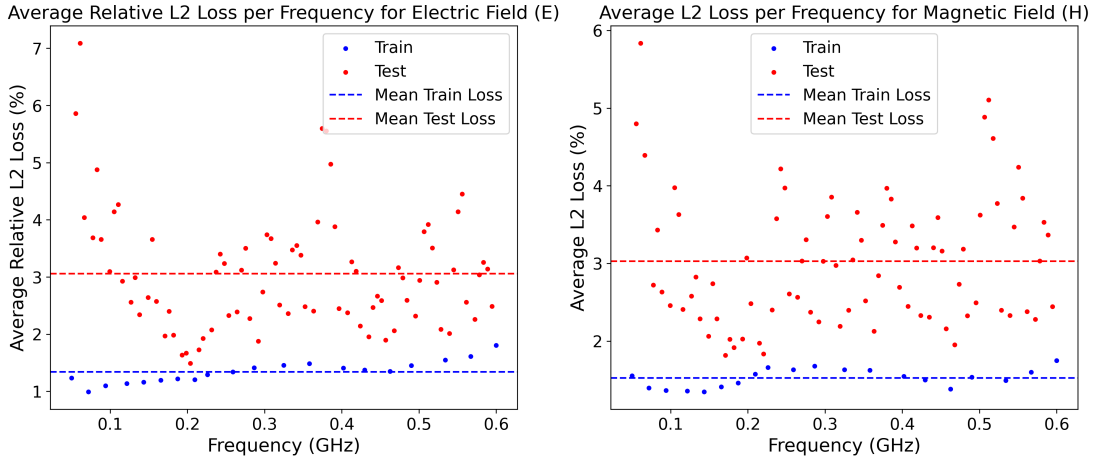


Figure 8: Scatter plots of relative L^2 losses for training (blue, 20 frequencies) and testing (red, 81 frequencies) selected using the acquisition function method from the frequency interval $[0.05, 0.6]$ GHz. The left plot shows average losses for electric field components (E_x, E_y, E_z), and the right for magnetic field components (H_x, H_y, H_z). Horizontal dotted lines mark the average losses for training and testing.

proposed DeepONet model for computing the integrated quantity, which is very sensitive to the accuracy of predict electromagnetic field from DeepONets.

5 Summary

In this study, we have developed a novel complex-valued DeepONet to address the challenge of operator learning for solutions expressed by complex numbers. This approach preserves the phase information of complex numbers, which offers a significant advantage over real-valued models for problems governed by inherently complex-valued equations. This study leads to important contributions that enhance the efficiency and applicability of neural operators for solving direct scattering problems governed by the time-harmonic Maxwell’s equations.

This works shows detailed numerical examples validating the effectiveness of the complex-valued DeepONet for predicting the total fields from inputs of the incident fields and the angular frequency. The proposed model beats the vanilla real-valued DeepONet in terms of prediction accuracy and maintains its performance when scaling to larger datasets. Additionally, the use of acquisition function to sample the frequency input space enables the model to perform well with only very limited training samples available.

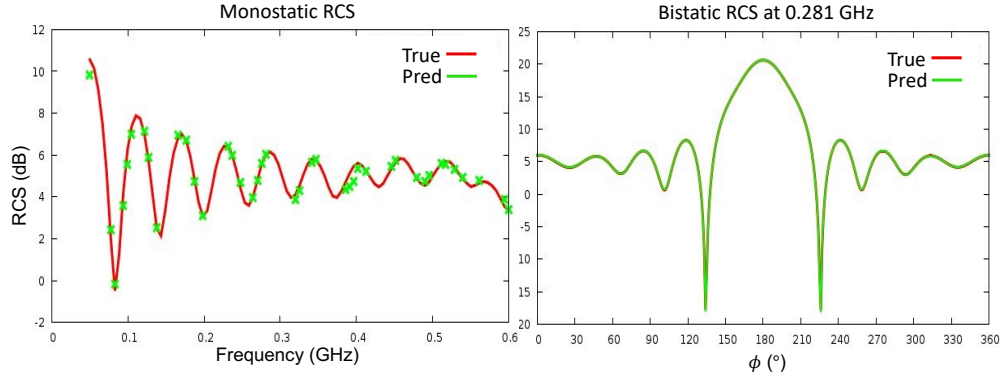


Figure 9: Monostatic and bistatic RCS results computed from DeepONet predictions (green) and compared to ground-truth Mie-series solutions (red). The monostatic RCS (left) is evaluated at 40 testing frequencies from the interval $[0.05, 0.6]$ GHz. The bistatic RCS (right) is calculated at a single frequency of 0.281 GHz and plotted against the azimuth angle ϕ .

This study not only extends the DeepONet for complex-valued data but also introduces a technique to combine multiple DeepONet models to impose the boundary conditions for PEC scatterers. We have additionally adapted the reparametrization and two-step training method of real-valued DeepONet to the complex valued DeepONet to enhance the efficiency of model training and accuracy.

This work sets the foundation for applying operator learning techniques to other complex-valued PDEs, e.g. Helmholtz equation, Schrodinger equations etc. A direction for further work would be to apply the method to model more complicated systems and reduce the computational cost of conventional numerical methods.

Acknowledgments

We gratefully acknowledge the financial support from Hypercomp Inc. This research was partially conducted using computational resources and services at the Center for Computation and Visualization (OSCAR) at Brown University. Additionally, we thank the AFOSR Grant FA9550-23-1-0671 for supporting the purchase of modern GPU hardware.

Data and code availability

The data and code related to the work will be made available through Github repository upon acceptance of the manuscript.

References

- [1] Anders Bondeson, Thomas Rylander, and Pär Ingelström. *Computational electromagnetics*. Springer, 2012.
- [2] Vinay Kumar Nassa. Wireless communications: Past, present and future. *Dronacharya Research Journal*, 50, 2011.
- [3] Tapan K Sarkar, Santana Burintramart, Nuri Yilmazer, Seunghyeon Hwang, Yu Zhang, Arijit De, and Magdalena Salazar-Palma. A discussion about some of the principles/practices of wireless communication under a maxwellian framework. *IEEE Transactions on antennas and propagation*, 54(12):3727–3745, 2006.
- [4] Bahman Zohuri. *Radar energy warfare and the challenges of stealth technology*. Springer, 2020.
- [5] Jacques R Ernst, Hansruedi Maurer, Alan G Green, and Klaus Holliger. Full-waveform inversion of crosshole radar data based on 2-d finite-difference time-domain solutions of maxwell’s equations. *IEEE transactions on geoscience and remote sensing*, 45(9):2807–2828, 2007.
- [6] Tim Bergmann, Johan OA Robertsson, and Klaus Holliger. Numerical properties of staggered finite-difference solutions of maxwell’s equations for ground-penetrating radar modeling. *Geophysical Research Letters*, 23(1):45–48, 1996.

- [7] Nirmal K Soni, Keith D Paulsen, Hamid Dehghani, and Alexander Hartov. Finite element implementation of maxwell's equations for image reconstruction in electrical impedance tomography. *IEEE Transactions on Medical Imaging*, 25(1):55–61, 2005.
- [8] Arman Afsari, Amin M Abbosh, and Yahya Rahmat-Samii. A rapid medical microwave tomography based on partial differential equations. *IEEE Transactions on Antennas and Propagation*, 66(10):5521–5535, 2018.
- [9] Jan S Hesthaven and Tim Warburton. Nodal high-order methods on unstructured grids: I. time-domain solution of maxwell's equations. *Journal of Computational Physics*, 181(1):186–221, 2002.
- [10] F Maggio, Giuseppe Mazzarella, and C Pitzianti. Least squares spectral element method for 2d maxwell equations in the frequency domain. *International Journal of Numerical Modelling: Electronic Networks, Devices and Fields*, 17(6):509–522, 2004.
- [11] Nikola B Kovachki, Samuel Lanthaler, and Andrew M Stuart. Operator learning: Algorithms and analysis. *arXiv preprint arXiv:2402.15715*, 2024.
- [12] Lu Lu, Pengzhan Jin, Guofei Pang, Zhongqiang Zhang, and George Em Karniadakis. Learning nonlinear operators via DeepONet based on the universal approximation theorem of operators. *Nature Machine Intelligence*, 3(3):218–229, 2021.
- [13] Nicolas Boullé and Alex Townsend. A mathematical guide to operator learning. *arXiv preprint arXiv:2312.14688*, 2023.
- [14] Tianping Chen and Hong Chen. Universal approximation to nonlinear operators by neural networks with arbitrary activation functions and its application to dynamical systems. *IEEE transactions on neural networks*, 6(4):911–917, 1995.
- [15] George Cybenko. Approximation by superpositions of a sigmoidal function. *Mathematics of control, signals and systems*, 2(4):303–314, 1989.
- [16] Kurt Hornik. Approximation capabilities of multilayer feedforward networks. *Neural networks*, 4(2):251–257, 1991.
- [17] Subhayan De, Matthew Reynolds, Malik Hassanaly, Ryan N King, and Alireza Doostan. Bi-fidelity modeling of uncertain and partially unknown systems using deeponets. *Computational Mechanics*, 71(6):1251–1267, 2023.
- [18] Lu Lu, Raphaël Pestourie, Steven G Johnson, and Giuseppe Romano. Multifidelity deep neural operators for efficient learning of partial differential equations with application to fast inverse design of nanoscale heat transport. *Physical Review Research*, 4(2):023210, 2022.
- [19] Amanda A Howard, Mauro Perego, George E Karniadakis, and Panos Stinis. Multifidelity deep operator networks. *arXiv preprint arXiv:2204.09157*, pages 1–28, 2022.
- [20] Min Zhu, Handi Zhang, Anran Jiao, George Em Karniadakis, and Lu Lu. Reliable extrapolation of deep neural operators informed by physics or sparse observations. *Computer Methods in Applied Mechanics and Engineering*, 412:116064, 2023.
- [21] Chensen Lin, Zhen Li, Lu Lu, Shengze Cai, Martin Maxey, and George Em Karniadakis. Operator learning for predicting multiscale bubble growth dynamics. *The Journal of Chemical Physics*, 154(10), 2021.
- [22] Peiyuan Gao, George Em Karniadakis, and Panos Stinis. Multiscale modeling framework of a constrained fluid with complex boundaries using twin neural networks. *arXiv preprint arXiv:2408.03263*, 2024.
- [23] Khemraj Shukla, Vivek Oommen, Ahmad Peyvan, Michael Penwarden, Nicholas Plewacki, Luis Bravo, Anindya Ghoshal, Robert M. Kirby, and George Em Karniadakis. Deep neural operators as accurate surrogates for shape optimization. *Engineering Applications of Artificial Intelligence*, 129:107615, 2024.
- [24] Shengze Cai, Zhicheng Wang, Lu Lu, Tamer A Zaki, and George Em Karniadakis. Deepm&mnet: Inferring the electroconvection multiphysics fields based on operator approximation by neural networks. *Journal of Computational Physics*, 436:110296, 2021.
- [25] Yue Hao, Patricio Clark Di Leoni, Olaf Marxen, Charles Meneveau, George Em Karniadakis, and Tamer A Zaki. Instability-wave prediction in hypersonic boundary layers with physics-informed neural operators. *Journal of Computational Science*, 73:102120, 2023.
- [26] Khemraj Shukla, Jasmine Ratchford, Luis Bravo, Vivek Oommen, Nicholas Plewacki, Anindya Ghoshal, and George Karniadakis. Deep operator learning-based surrogate models for aerothermodynamic analysis of aedc hypersonic waverider. *arXiv preprint arXiv:2405.13234*, 2024.
- [27] Georgios Kissas, Jacob H Seidman, Leonardo Ferreira Guilhoto, Victor M Preciado, George J Pappas, and Paris Perdikaris. Learning operators with coupled attention. *Journal of Machine Learning Research*, 23(215):1–63, 2022.

- [28] QiZhi He, Mauro Perego, Amanda A Howard, George Em Karniadakis, and Panos Stinis. A hybrid deep neural operator/finite element method for ice-sheet modeling. *Journal of Computational Physics*, 492:112428, 2023.
- [29] Danxiang Wang, Fangfang Xie, Tingwei Ji, Xuhui Meng, and Yao Zheng. Learning mappings of thermal updraft fields under unknown operating conditions using a deep operator network. *Physics of Fluids*, 36(6), 2024.
- [30] Somdatta Goswami, Minglang Yin, Yue Yu, and George Em Karniadakis. A physics-informed variational deepnet for predicting crack path in quasi-brittle materials. *Computer Methods in Applied Mechanics and Engineering*, 391:114587, 2022.
- [31] Junyan He, Seid Koric, Shashank Kushwaha, Jaewan Park, Diab Abueidda, and Iwona Jasiuk. Novel deepnet architecture to predict stresses in elastoplastic structures with variable complex geometries and loads. *Computer Methods in Applied Mechanics and Engineering*, 415:116277, 2023.
- [32] Feliks Aleksandrovich Berezin and Mikhail Shubin. *The Schrödinger Equation*, volume 66. Springer Science & Business Media, 2012.
- [33] Barton Zwiebach. *Mastering quantum mechanics: essentials, theory, and applications*. MIT Press, 2022.
- [34] Oliver G Ernst and Martin J Gander. Why it is difficult to solve helmholtz problems with classical iterative methods. *Numerical analysis of multiscale problems*, pages 325–363, 2011.
- [35] Sachin Munshi and Rongwei Yang. Complex solutions to maxwell’s equations. *Complex Analysis and its Synergies*, 8(1):2, 2022.
- [36] James A Reggia. Generalizing maxwell’s equations to complex-valued electromagnetic fields. *Physica Scripta*, 99(1):015513, 2023.
- [37] Yuyao Chen, Lu Lu, George Em Karniadakis, and Luca Dal Negro. Physics-informed neural networks for inverse problems in nano-optics and metamaterials. *Optics express*, 28(8):11618–11633, 2020.
- [38] Peter R Wiecha, Arnaud Arbouet, Christian Girard, and Otto L Muskens. Deep learning in nano-photonics: inverse design and beyond. *Photonics Research*, 9(5):B182–B200, 2021.
- [39] Chengke Zhu, Hongxia Ye, and Bin Zhan. Fast solver of 2d maxwell’s equations based on fourier neural operator. In *2021 Photonics & Electromagnetics Research Symposium (PIERS)*, pages 1635–1643. IEEE, 2021.
- [40] Joowon Lim and Demetri Psaltis. Maxwellnet: Physics-driven deep neural network training based on maxwell’s equations. *Apl Photonics*, 7(1), 2022.
- [41] Taehwan Kim and Tülay Adali. Complex backpropagation neural network using elementary transcendental activation functions. In *2001 IEEE International Conference on Acoustics, Speech, and Signal Processing. Proceedings (Cat. No. 01CH37221)*, volume 2, pages 1281–1284. IEEE, 2001.
- [42] Md Faijul Amin, Muhammad Ilias Amin, Ahmed Yarub H Al-Nuaimi, and Kazuyuki Murase. Wirtinger calculus based gradient descent and levenberg-marquardt learning algorithms in complex-valued neural networks. In *International Conference on Neural Information Processing*, pages 550–559. Springer, 2011.
- [43] Sindy Löwe, Phillip Lippe, Maja Rudolph, and Max Welling. Complex-valued autoencoders for object discovery. *arXiv preprint arXiv:2204.02075*, 2022.
- [44] Patrick Virtue, X Yu Stella, and Michael Lustig. Better than real: Complex-valued neural nets for mri fingerprinting. In *2017 IEEE international conference on image processing (ICIP)*, pages 3953–3957. IEEE, 2017.
- [45] Md Faijul Amin, Ramasamy Savitha, Muhammad Ilias Amin, and Kazuyuki Murase. Complex-valued functional link network design by orthogonal least squares method for function approximation problems. In *The 2011 International Joint Conference on Neural Networks*, pages 1489–1496. IEEE, 2011.
- [46] Tohru Nitta. An extension of the back-propagation algorithm to complex numbers. *Neural Networks*, 10(8):1391–1415, 1997.
- [47] Tomi Huttunen, Peter Monk, and Jari P Kaipio. Computational aspects of the ultra-weak variational formulation. *Journal of Computational Physics*, 182(1):27–46, 2002.
- [48] Tomi Huttunen, Matti Malinen, and Peter Monk. Solving maxwell’s equations using the ultra weak variational formulation. *Journal of Computational Physics*, 223(2):731–758, 2007.
- [49] Tomi Huttunen, Peter Monk, Vijaya Shankar, and William Hall. High-order ultra-weak variational formulation for maxwell equations. In *2018 IEEE International Conference on Computational Electromagnetics (ICCEM)*, pages 1–3. IEEE, 2018.
- [50] T Luostari, T Huttunen, and P Monk. Improvements for the ultra weak variational formulation. *International Journal for Numerical Methods in Engineering*, 94(6):598–624, 2013.

- [51] Timo Lähivaara, William F Hall, Matti Malinen, Dale Ota, Vijaya Shankar, and Peter Monk. A high-order ultra-weak variational formulation for electromagnetic waves utilizing curved elements. *IEEE Transactions on Antennas and Propagation*, 2024.
- [52] ChiYan Lee, Hideyuki Hasegawa, and Shangce Gao. Complex-valued neural networks: A comprehensive survey. *IEEE/CAA Journal of Automatica Sinica*, 9(8):1406–1426, 2022.
- [53] J Agustin Barrachina. Negu93/cvnn: Complex-valued neural networks, November 2023.
- [54] Julia Ling, Reese Jones, and Jeremy Templeton. Machine learning strategies for systems with invariance properties. *Journal of Computational Physics*, 318:22–35, 2016.
- [55] Julia Ling, Andrew Kurzawski, and Jeremy Templeton. Reynolds averaged turbulence modelling using deep neural networks with embedded invariance. *Journal of Fluid Mechanics*, 807:155–166, 2016.
- [56] Sanghyun Lee and Yeonjong Shin. On the training and generalization of deep operator networks. *SIAM Journal on Scientific Computing*, 46(4):C273–C296, 2024.
- [57] Ethan Pickering, Stephen Guth, George Em Karniadakis, and Themistoklis P Sapsis. Discovering and forecasting extreme events via active learning in neural operators. *Nature Computational Science*, 2(12):823–833, 2022.